Acta Materialia 215 (2021) 117054

Contents lists available at ScienceDirect

Acta Materialia

journal homepage: www.elsevier.com/locate/actamat

Full length article

Spinodal Decomposition in Nanocrystalline Alloys

Xuyang Zhou[a,b], Reza Darvishi Kamachali[c,*], Brad L. Boyce[d], Blythe G. Clark[d], Dierk Raabe[b], Gregory B. Thompson[a,*]

[a] The University of Alabama, Department of Metallurgical Materials Engineering, 35487 Tuscaloosa, AL, USA
[b] Max-Planck-Institut für Eisenforschung GmbH, Max-Planck-Straße 1, 40237 Düsseldorf, Germany
[c] Federal Institute for Materials Research and Testing (BAM), Unter den Eichen 87, 12205 Berlin, Germany
[d] Sandia National Laboratories, 87123 Albuquerque, NM, USA

ARTICLE INFO

Article history:
Received 9 February 2021
Revised 31 May 2021
Accepted 1 June 2021
Available online 7 June 2021

ABSTRACT

For more than half a century, spinodal decomposition has been a key phenomenon in considering the formation of secondary phases in alloys. The most prominent aspect of the spinodal phenomenon is the lack of an energy barrier on its transformation pathway, offering an alternative to the nucleation and growth mechanism. The classical description of spinodal decomposition often neglects the influence of defects, such as grain boundaries, on the transformation because the innate ability for like-atoms to cluster is assumed to lead the process. Nevertheless, in nanocrystalline alloys, with a high population of grain boundaries with diverse characters, the structurally heterogeneous landscape can greatly influence the chemical decomposition behavior. Combining atom-probe tomography, precession electron diffraction and density-based phase-field simulations, we address how grain boundaries contribute to the temporal evolution of chemical decomposition within the miscibility gap of a Pt-Au nanocrystalline system. We found that grain boundaries can actually have their own miscibility gaps profoundly altering the spinodal decomposition in nanocrystalline alloys. A complex realm of multiple interfacial states, ranging from competitive grain boundary segregation to barrier-free low-dimensional interfacial decomposition, occurs with a dependency upon the grain boundary character.

1. Introduction

Alloys of two or more different types of atoms can produce more than one phase, with the formation of these 'secondary phases' providing mechanisms for strengthening and/or stabilizing the microstructure [1-4]. Understanding how solute elements then partition among phases and crystal defects is essential in controlling how such phases form within these microstructures [3,5-7]. In the case of nanocrystalline alloys, where strength is intimately connected to smaller grain sizes (i.e., the Hall-Petch effect [8,9]), the ability for chemical partitioning to retard grain coarsening is critical [10-12], with this capillarity-driven problem being a general response observed in many fine-scaled materials [13]. In metal alloys, specific solutes can then phase separate from the matrix into the interfacial boundary reducing the thermodynamic driving forces for such coarsening [11,12,14-20]. Alternatively, solutes can cluster and precipitate out as distinct, secondary phases that kinetically retard the boundary, a phenomenon known as Zener pinning [3,21,22]. In either case, understanding how solute atoms evolve in the boundary gives insights into the microstructural stability in these materials. In many alloys, this elemental phase separation is driven by immiscibility between their constituent elements.

In alloys that exhibit a miscibility gap, the phase separation process can occur through a barrier-free transformation referred to as spinodal decomposition [23,24]. The term 'barrier-free' infers that the secondary phase does not necessarily overcome an interfacial energy barrier as required in nucleation mechanisms. This spinodal phenomena spans glaze formation in ceramic pottery to precipitation in steels [25,26]. Historically, when describing spinodal decomposition, the effect of structural defects on the transformation pathway are neglected because of the innate ability for like-atoms to cluster; this is in stark contrast to the mechanism of nucleation and growth phase transformations where defects readily contribute to the energetics of where and how secondary phases form by reducing the interfacial energy barrier [23,24]. In a nanocrystalline alloy, with a high density of grain boundaries (GBs), the influence of these structural defects can no longer be ignored in an immiscible alloy that has a miscibility gap, since they can have a significant influence on the solute partitioning and transformation pathway for spinodal decomposition [27,28]. In the

* Corresponding author.
E-mail addresses: reza.kamachali@bam.de (R. Darvishi Kamachali), gthompson@eng.ua.edu (G.B. Thompson).

https://doi.org/10.1016/j.actamat.2021.117054
1359-6454/

work by da Silva *et al.* [27], defects including GBs and dislocations were shown to alter the spatial location and behavior of the decomposition behavior from the bulk interior. Arguably, this chemical decomposition in nanoscale materials with a high density of varied GB characters is neither well characterized nor understood.

For many decades, the ability to ascertain the solute evolution in a GB has been hindered by the need for high chemical sensitivity to detect the solute atoms coupled with a high spatial resolution to decipher the boundary structure [29-32]. Here, we have overcome these experimental challenges through cross-correlative microscopy using atom probe tomography (APT), to capture the chemical signature of the solute on the GB-plane, with precession electron diffraction (PED) identifying the structural boundary's misorientation [29,30]. Using this cross-correlative method [29,30], we have studied an immiscible nanocrystalline Pt-11Au (0.11 atomic fraction Au) alloy, which has a miscibility gap, and directly linked the experimental characterization to a new density-based phase-field (DPF) model [33]. In this model, we are able to elucidate the relative effect of individual GB character on the barrier-free interfacial decomposition that captures and explains the temporal evolution of segregation and decomposition observed experimentally over a network of nanometer distanced GBs.

While various techniques have been applied to simulate the interaction between GBs and solutes, each method has its own limitations. For example, first-principles [34-36] and atomistic [37-40] simulations capture interfacial solute decoration, but often struggle in summarizing collective effects of GBs in the larger context of the microstructure. In other models that capture a larger field-of-view perspective [16,17,41-46], simultaneous consideration of segregation into multiple coexisting GBs with various characters has been challenging. Using the DPF model with experimental integration, we enable a direct consideration of multiple GBs characterized in our nanocrystalline microstructure using this Pt-Au nanocrystalline alloy as our case system. This alloy offers several advantages. First, the noble metals reduce the complexity of reactions with impurities and the environment when anneal ensuring a 'clean' experimental system to address the partitioning and decomposition behavior within the nanostructure [47,48]. Secondly, the alloy has been studied as a model system with respect to nanocrystalline stability [40,48-50] as well as mechanical behavior [49], providing context and comparison to other investigations. While those studies have been paramount in revealing GB anisotropic partitioning as will be shortly shown, their focus on grain coarsening through experimental electron microscopy and molecular dynamic simulations largely address the property outcomes of the solute in the boundary. In this work, we centrally focuse on how the solute evolves to and within the boundary when the alloy itself has a thermodynamic miscibility gap. We found that grain boundaies can actually have their own miscibility gaps and corresponding spinodal decomposiotion behavior. Our results reveal a very complex realm of multiple interfacial states, ranging from segregation to interfacial chemical decomposition, the nature of which relies on the nanocrystalline alloy's GB characters giving new insights into a traditional phase transformation

2. Materials and Methods

2.1. Sample Preparation

An alloyed Pt-11Au (0.11 atomic fraction Au) thin film was sputter-deposited from 99.9 % pure Pt and Au elemental targets in a stainless steel magnetron-sputtering system. The targeted composition was achieved through co-sputtering two elemental targets at different power settings yielding the appropriate deposition rate. The base vacuum pressure prior to deposition was $< 6 \times 10^{-6}$ Pa. During sputtering, ultra-high purity argon was flowed as the working gas to maintain a pressure of 1.3 Pa. The film was grown to an approximate thickness of 2 μm onto 300 μm thick silicon [100] substrates that had a native surface oxide. To prevent any deleterious interactions between the film and substrate with subsequent annealing, the Pt(Au) films were detached from the substrate. The films were then annealed at 700 K for 4, 24, or 720 hours (h) in a custom constructed vacuum annealing chamber that consisted of quartz tube evacuated by a turbomolecular pump to a base pressure of $< 1 \times 10^{-6}$ Pa that was inserted in a cylindrical (tube) furnace.

2.2. Diffraction Analysis

The phase and microstructure of these samples were examined by scanning transmission electron microscopy ((S)TEM) using a FEI Tecnai F20 operated at 200 kV. The TEM samples were prepared in the plan-view orientation (electron beam normal to the substrate) by a focused ion beam (FIB) lift-out technique using either a FEI Quanta 3D or Tescan Lyra dual electron FIB - scanning electron microscope (SEM). Here, the wedge was rotated 90° before attaching to the TEM grid and then FIB milled to remove some portion of the film until a segment of the foil was $<$ 100 nm enabling it to be electron transparent. The TEM composition spectrum and mapping measurements were done by Energy-Dispersive X-ray Spectroscopy (EDXS) using an EDAX silicon drift detector (SDD). Grain sizes and orientation distributions were quantified by PED using a NanoMEGAS ASTAR platform.

The PED scans were obtained with a 0.3° precession angle at a scanning step size of 3 nm over a 2 μm $\times$ 0.5 μm region of interest (ROI) in the in-plane orientation. After scanning, the data was converted for analysis for the TSL OIM Analysis 8 software package. Grain-based misorientation analyses were employed to identify the grains with varying local misorientations. To improve the reliability of the PED data, grains comprising fifty or fewer pixels within 1° grain angular tolerance were automatically removed from the maps using the grain dilation function in the TSL software.

2.3. APT Analysis

The composition and element distributions of the alloy films were characterized by APT performed in a Cameca Instruments Local Electrode Atom Probe (LEAP) 5000 XS. A FIB lift-out technique to prepare the APT tips was used with the aforementioned FEI Quanta 3D dual beam FIB-SEM. The FIB extracted tips were mounted onto a Si half grid TEM holder and sharpened into needle-like geometries necessary for field evaporation with a 5 keV clean-up step to remove Ga^+ implanted surface damage using a Tescan Lyra FIB- Field Emission SEM. The tips, attached to the Si half grid, were mounted onto a Hummingbird TEM holder that was then placed into the Tecnai F20 for imaging. The grain-to-grain mapping of the tip was again conducted using the PED technique described above with the beam precessed at 0.3° at a scanning step size of 2 nm.

The tips were field evaporated in the LEAP using laser pulse energies between 250-350 pJ at a pulse repetition rate of 200 kHz for a 1.2% atoms per pulse detection rate. The specimen temperature set point of the tips in the LEAP was set at 40 K. The collected atom probe data was reconstructed via the IVAS 3.8.4 software platform. For further details on the PED and APT cross-correlative methodology, the reader is referred to Ref. [30].

2.4. Grain Boundary Composition Quantification

GB concentration maps of the APT datasets were used to visualize and quantify the solute segregation within the GB planes [51,52]. In this approach, we triangularly meshed the GB planes

with a unit size of ~ 4 nm^2. Using a distance-to-center of mass (DCOM) approach, the vertices were iteratively fitted to the GB. Once fitted, a centroid Voronoi tessellation (CVT) method produced an even distribution of verities on the mesh. A MATLAB (Mathworks Inc.) code, modified from the work in reference [51] calculated the ladder diagram for each vertex necessary to compute the Gibbsian interfacial excess. Benefiting from this approach, the accurate location of a vertex enabled a carefully determined local concentration quantification. Overlaying the PED GB map to the APT reconstructed image that was specifically correlated to each GB, the solute concentration to the GB character were matched.

2.5. Density-based Phase-Field Model

Previous phase-field simulations of segregation in a Pt-Au nanocrystalline structure have been conducted by assuming isotropic GB properties [53]. Here, we expand on these ideas by considering multiple coexisting GBs of various characters. To do so, we apply a density-based phase-field approach that allows an approximation of the GB environment with reference to its corresponding bulk material [33]. The core idea of this model is the use of a relative atomic density parameter, ρ, that enables a mean-field approximation of the GB solid solution with reference to the defect-free bulk material ($\rho = 1$), while the atomic density and solute concentration gradient energy contributions account for the GB's through-thickness structural and compositional inhomogeneities, respectively. Considering both structural and compositional inhomogeneities in studying GB segregation, Wang and coworkers [41] proposed using the coordination number as the key structural property. Here, the continuum atomic density parameter can be interpreted as a coarse-grained description of the coordination number [33]. The density-based model has been successfully applied for studying Mn segregation in the FeMn binary system [28], co-segregation in a FeMnNiCrCo alloy [54] and the calculation of GB phase diagrams for ternary steels [55].

The atomic density parameter ρ is normalized by the bulk density such that $\rho = 1$ for the homogeneous, defect-free bulk structure and across a given GB, the density field varies as $\rho^{GB} \leq \rho < 1$, with the subtle details of the boundary assessed by assigning its GB density ρ^{GB} at the GB-plane (at the center of the GB). In principle, the atomic density within a GB-plane will fluctuate [48]; however, in the present study, we evaluate the average constant GB density value, ρ^{GB}, for each given GB. Accordingly, a monotonic function can be used to readily relate GB density, energy and misorientation angle, as will be further discussed below. The density-based Gibbs free energy of a pure substance i is derived as

$$G_i(\rho) = \rho^2 E_i^B + \rho\left(G_i^B - E_i^B\right) + \frac{\kappa_i^\rho}{2}(\nabla\rho)^2 \tag{1}$$

where E_i^B and $G_i^B$are the potential energy and the Gibbs free energy of the corresponding homogeneous bulk phase, κ_i^ρ is the atomic density gradient energy coefficient, and the Gibbs free energy functional is given by $\mathcal{G}_i = \int G_i(\rho)\ \mathrm{d}V$. For our assessments, we first consider a flat GB separating two infinitely large grains. Over the finite GB region and normal to the GB-plane, a symmetric density profile appears with its minimum at the center, $\rho = \rho^{GB}$, with the continuity of such a coarse-grained density profile confirmed using atomistic simulations [28]. At equilibrium, $\frac{\delta \mathcal{G}_i}{\delta \rho} = 0$ (here δ indicates the functional derivative) and the equilibrium density profile reads

$$\rho_{eq}(x) = \left(\frac{1+\rho^{GB}}{2}\right) - \left(\frac{1-\rho^{GB}}{2}\right)\cos\left(\frac{\pi x}{\eta}\right) \quad \text{for} \quad -\eta \leq x \leq \eta \tag{2}$$

with $\eta = \pi\sqrt{\frac{\kappa_{Pt}^\rho}{-2E_{Pt}^B}}$ being the GB half-width. Since our system of interest is Pt-rich, we assume the GB to be initially in a pure Pt system. Therefore, the GB energy is obtained by $\gamma = 2\int_0^\eta (G_{Pt}(\rho) - G_{Pt}^B)\ dV$. Inserting Eqs. (1) and (2) in this relation, we obtain

$$\gamma = \alpha_0\left(1-\rho^{GB}\right)^2 \tag{3}$$

where $\alpha_0 = \frac{\pi}{4V_m}\sqrt{-2E_{Pt}^B\kappa_{Pt}^\rho}$ is a material constant with V_m the molar volume of Pt. Equation (3) reveals that as the GB structure deviates larger from the bulk, i.e., ρ^{GB} deviates more from 1, the GB energy γ monotonically increases. The GB density ρ^{GB} is then related to the average in-plane GB excess volume ΔV by $\Delta V \propto (1-\rho^{GB})$ [33], which is commonly used as a parameter for describing the deviation in the GB structure from that of the corresponding defect-free bulk structure (see, for instance, Ref. [56] and references therein). This is further related to the GB energy and misorientation angle θ as discussed in previous studies [57,58]. With the exemption of special GBs (coincident site lattices, CSLs), a high-angle GB (HAGB, greater than 15°) then possesses a higher excess free volume and energy than that of a low-angle GB (LAGB, lower than 15°).

Eq. (3) is now used to relate GB misorientation and energy with the relative GB density values [33,54], so that the effect of GB character can be included in the phase-field simulations. Here we chose a phenomenological approximation

$$\rho^{GB} = 1 - \frac{\sin\theta}{4} \tag{4}$$

to relate the average GB density and GB misorientation angle. With $V_m = 9.1 \times 10^{-6}\ m^3\ mol^{-1}$, $E_{Pt}^B = -5.6 \times 10^4\ J\ mol^{-1}$ [59] and $\kappa_{Pt}^\rho = 2.2 \times 10^{-14}\ J\ m^2\ mol^{-1}$ for Pt atoms, we obtain $\eta = 1.4\ nm$ and $\alpha_0 = 1.7\ J\ m^{-2}$. Furthermore, we consider a range of GB energies $\theta \in [0,\ \pi/3]$ that gives GB energies $\gamma_{Pt} \in [0,\ 1.5]\ J\ m^{-2}$ [60]. The relations from these inputs are plotted in Fig. 1 A-C. With the exemption of special GBs, Eq. (3) yields higher GB energies (lower GB densities) for the HAGBs and lower GB energies (higher GB densities close to 1) for the LAGBs. The relative values of the GB densities now enable us to study the relative segregation and phase decomposition behavior among multiple coexisting GBs of various characters within our nanocrystalline material.

For the binary Pt-Au system, we need to further cast the density-based formulation of Eq. (1) into the regular solution model [33]

$$\begin{aligned} &G(X_{Au}, \rho, \nabla X_{Au}, \nabla\rho) \\ &\quad = X_{Pt}\left[\rho^2 E_{Pt}^B + \rho\left(G_{Pt}^B - E_{Pt}^B\right) + \frac{\kappa_{Pt}^\rho}{2}(\nabla\rho)^2\right] \\ &+X_{Au}\left[\rho^2 E_{Au}^B + \rho\left(G_{Au}^B - E_{Au}^B\right) + \frac{\kappa_{Au}^\rho}{2}(\nabla\rho)^2\right] \\ &+\ \rho^2\Omega_{PtAu}X_{Pt}X_{Au} - T\Delta S^{\text{Config}} + \frac{\kappa_X}{2}(\nabla X_{Au})^2. \end{aligned} \tag{5}$$

where, in addition to the (structural) atomic density gradients, we also have the chemical gradient energies within our binary system [61], $\frac{\kappa_X}{2}(\nabla X_{Au})^2$. The concentration gradient energy is an important component for studying phase decomposition in the Pt-Au system, particularly at the GBs where chemical inhomogeneities are expected because of segregation. In the current formulation, we approximated the GB environment, relative to its parent homogeneous bulk phase, with a dimensionless mean-field atomic density parameter that allowed us to use available bulk thermodynamic data as inputs. In doing so we benefit from having spatial gradient energy contributions to describe the structural and chemical variations across the system. To that end, Grolier *et al.* [62] have

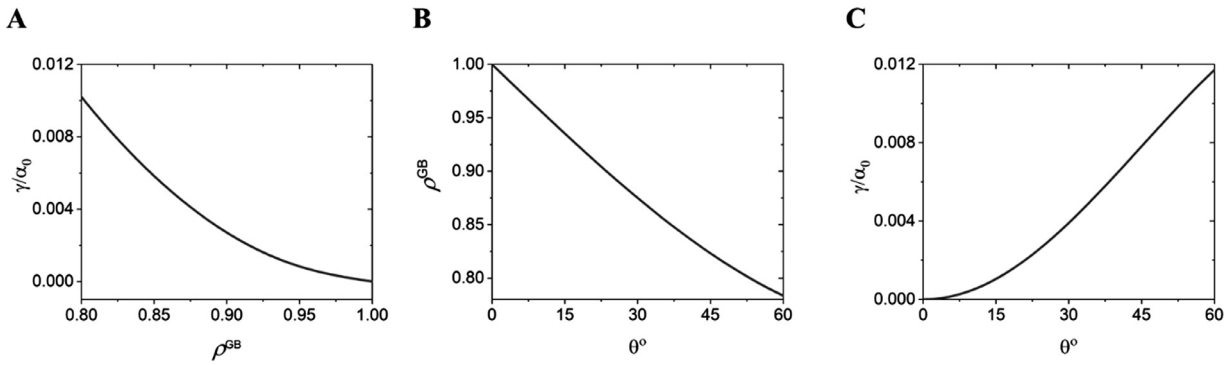

Fig. 1. The relationships of **A** the GB energy (γ) and GB atomic density, **B** GB atomic density (ρ^{GB}) and misorientation angle (θ) and **C** GB energy (γ) with misorientation angle (θ). For large deviations from the bulk structure, i.e., lower GB density and higher misorientation angles, a larger GB energy will be obtained according to Eqs. (3) and (4). Here ρ^{GB} is less than 1. When atomic density equals 1, it represents the bulk structure. This monotonic trend is used to capture the relative segregation behavior of various GBs of different characters.

assessed the bulk thermodynamic data for the binary Pt-Au system in which the enthalpy of mixing for this alloy extends to the second term in the Redlich-Kister polynomial:

$$\Omega_{PtAu} = \Omega_0 + \Omega_1 (X_{Pt} - X_{Au}) \tag{6}$$

with $\Omega_0 = 11625 + 8.3104 \times (T - 273.15)$ and $\Omega_1 = 12616 + 5.8186 \times (T - 273.15)$ [62]. The configurational entropy of mixing for a statistical solid solution in Eq. (5) reads as

$$\Delta S^{\text{Config}} = -R[X_{Pt} \ln X_{Pt} + X_{Au} \ln X_{Au}] \tag{7}$$

with R being the universal gas constant. The Gibbs free energy functional of the mixture is then given by $\mathcal{G} = \int G(X_{Au}, \rho, \nabla X_{Au}, \nabla \rho) \mathrm{d}V$. We now solve for the concentration and atomic density fields using the Cahn-Hilliard and Allen-Cahn equations, respectively [28]:

$$\dot{X}_{Au} = -\nabla \cdot \mathbf{J}_{Au} = \nabla \cdot \left[M_{Au} X_{Au} \nabla \frac{\delta \mathcal{G}}{\delta X_{Au}} \right] \tag{8}$$

$$\dot{\rho} = -L \frac{\delta \mathcal{G}}{\delta \rho} \tag{9}$$

where $\frac{\delta \mathcal{G}}{\delta q} = \frac{\partial \mathcal{G}}{\partial q} - \nabla \frac{\partial \mathcal{G}}{\partial \nabla q}$ defines the functional derivative (q : ρ or X_{Au}). Here, M_{Au} is the atomic mobility of Au atoms and L is a positive kinetic coefficient. As a diffusion-controlled process, the kinetics of segregation and phase separation are governed by the mobility of Au solute atoms while the atomic density field evolves much faster by atomic bond relaxation in the elastic regime. For $T = 700\ K$, we use $M_{Au} = 6.48 \times 10^{-15} mol\ m^2 J^{-1} s^{-1}$ [63]. To assure the diffusion-controlled kinetics, a large value $L = 10^{-7} mol\ J^{-1} s^{-1}$ is chosen compared to the atomic mobility. All the thermodynamic data are taken from Ref. [62]. The concentration gradient coefficient, κ_X, can be related to the spinodal phase separated interfacial energy, γ_I, based on the Cahn-Hilliard relationship [61]

$$\gamma_I = \sqrt{2\kappa_X} \int_{X_{Au}^l}^{X_{Au}^h} \sqrt{\Delta G^B(X_{Au})} dX_{Au} \tag{10}$$

where X_{Au}^l and X_{Au}^h are the corresponding compositions of the miscibility gap at $T = 700$ K and $\Delta G^B(X_{Au})$ is the free energy difference between a homogeneous Pt-Au alloy and the phase-separated mixture given by the common-tangent construction. For simplicity, we assume that $\kappa_{X_{Au}}$ does not depend on the composition. Assuming $\gamma_I = 0.05\ J\ m^{-2}$ and using the data in [62], we obtain $\kappa_X = 5.0 \times 10^{-13}\ J\ m^2 mol^{-1}$.

Finally, in order to perform the three dimensional (3D) full-field simulations of the Pt-11Au system, the two-dimensional (2D) PED information of the GB structure obtained from the experiments were used to extract a domain of $80 \times 100\ nm^2$ with all of the GB misorientation angles. From that experimental dataset, a direct 3D simulation box of $80 \times 100 \times 100\ nm^3$ with a columnar grain structure, which formed through the thickness of these films, has been generated based on the 2D structural input with a spatial resolution of $dx = 1$ nm and initialized with $X_{Au} = 0.11 \pm 0.01$ (for random noise). The GB densities were set as a function of the misorientation angles using Eq. (4) and experimental data. Elsewhere in the simulation domain, the density field was intially set equal to 1, *i.e.*, the bulk atomic density. An OpenMP parallel C++ program with a finite difference scheme and an adaptive time stepping was developed to solve Eqs. (8) and (9) numerically, with a periodic boundary condition applied.

3. Results

3.1. Microstructure Evolution

When sputter deposited, the nanocrystalline Pt-11Au alloy formed a solid solution face centered cubic (FCC) phase, confirmed by electron diffraction. The various PED grain maps, Fig. 2A, histogram of the grain size distribution, Fig. 2B, and cumulative grain size area distributions, Fig. 2C, reveal the nano-granular evolution for the various annealing times. The PED maps, which were taken normal to the growth direction, revealed a strong {111} texture. This would be consistent with such planes being the low surface energy orientation for FCC metals that form upon sputter deposition. Upon annealing at 700 K, we noted a shift to a slightly larger grain size distribution from the as-deposited state after 4 h; however, the grain size distribution is still relatively narrow indicated by the steep slope of the area size distribution versus grain size. Interestingly, this distribution in size then slightly refines (even below the as-deposited condition) with continual annealing for 24 h and 720 h. Nonetheless, the average grain sizes, Fig. 2D, are all within one standard deviation indicating that such changes are not statistically significant. The Pt(Au) alloy has been reported to be a nanocrystalline stabilized alloy [48], with our results confirming this previous study. The PED data from Fig. 2A also provides information on the GB misorientation (hence GB types). Fig. 2E are histograms of these GBs for as-deposited and different annealing states at 700 K. From these plots, GBs with misorientation angles between $2^\circ - 15^\circ$ were defined as LAGBs and GB misorientations greater than 15° as either random HAGBs or CSL special character boundaries. Of the CSL boundaries, the $\Sigma 3$ boundaries are explicitly extracted from this grouping and plotted independently in Fig. 2E as they comprised the highest CSL fraction of those boundaries. All other CSL boundaries, such as $\Sigma 7$ and $\Sigma 11$, were grouped under the CSL designation. In general, there is no

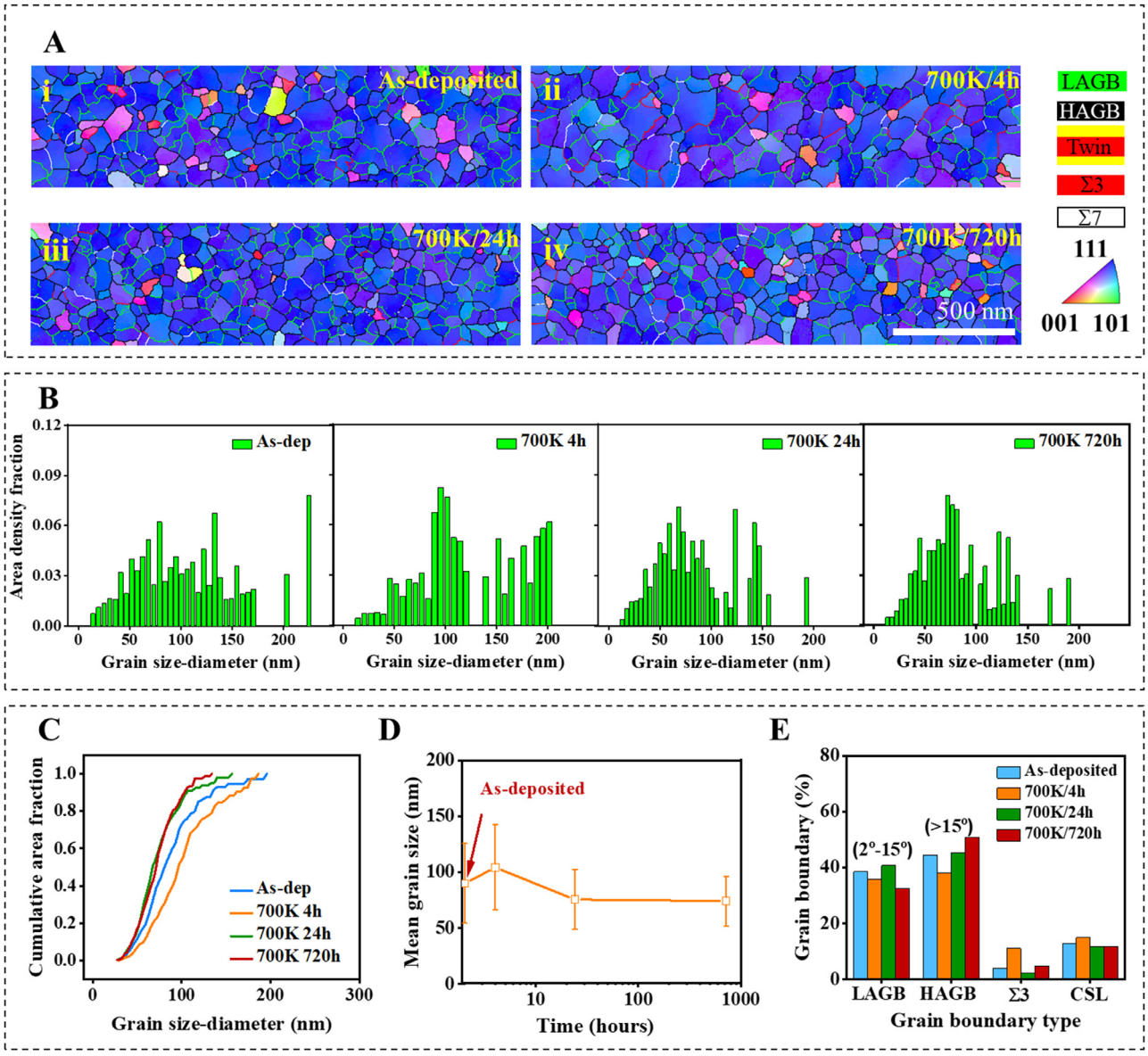

Fig. 2. **A** PED orientation and grain boundary maps for the (i) as-deposited (261 grains) (ii) 700 K/4 h (195 grains) (iii) 700 K/24 h (335 grains) (iv) 700 K/720 h (332 grains) annealed Pt-11Au films. **B** histogram of grain size distribution and **C** cumulative area fraction of grains shown in A **D** grain size evolution as a function of time and annealing temperature. Error bars in D indicate standard deviation. **E** histogram plots of the grain boundary types as a function of annealing time.

significant change in GB types for the 700 K annealed samples as a function of time.

3.2. Pre-annealed Chemical Structure

In the as-deposited state, the APT datasets, Fig. 3A and B, confirmed that the alloy was chemically homogeneous using a nearest neighbor algorithm [64,65]. In both Fig. 3A and B, the clear presence of two crystallographic poles is evident in either the isodensity surface or atom map distribution, with such features being a result of trajectory reconstruction aberrations from the poles [66-68]. While regions at and near these aberrations inhibit accurate chemical analysis, the presence of poles provides structural evidence for the presence of different grains within the field-of-view and serve as a guide in identifying the GB locations. These boundaries are highlighted by their own iso-density surface variations from the pole as shown in Fig. 3A and can be inferred from the density changes in the atom map in Fig. 3B. The chemical profile from GB1, Fig. 3C, taken from a $\pi \times 7^2 \times 20\ nm^3$ cylindrical volume, does not reveal any distinct Au segregation to this GB.

Similar compositional profiles were noted in the other GBs for this sample. Fig. 3D is the atom map of a $20 \times 20 \times 20\ nm^3$ cube cropped from the APT data of the as-deposited Pt-11Au sample, with this region chosen away from the poles (where the reconstruction aberrations are the strongest). The Au-Au nearest-neighbor distributions in Fig. 3E [64,65] reveals that the randomized data is overlapped with the raw data, indicating a random distribution of Au atoms in the Pt lattice. Being in a random solid solution provides an ideal initial condition to then characterize how the solute evolves out of solution and into the GBs in this nanocrystalline alloy.

3.3. Solute Partitioning Behavior

As evident in the results for the as-deposited film, where the solute is in solution, the APT technique provides an ideal means to identify and spatially resolve the solute upon phase separation.

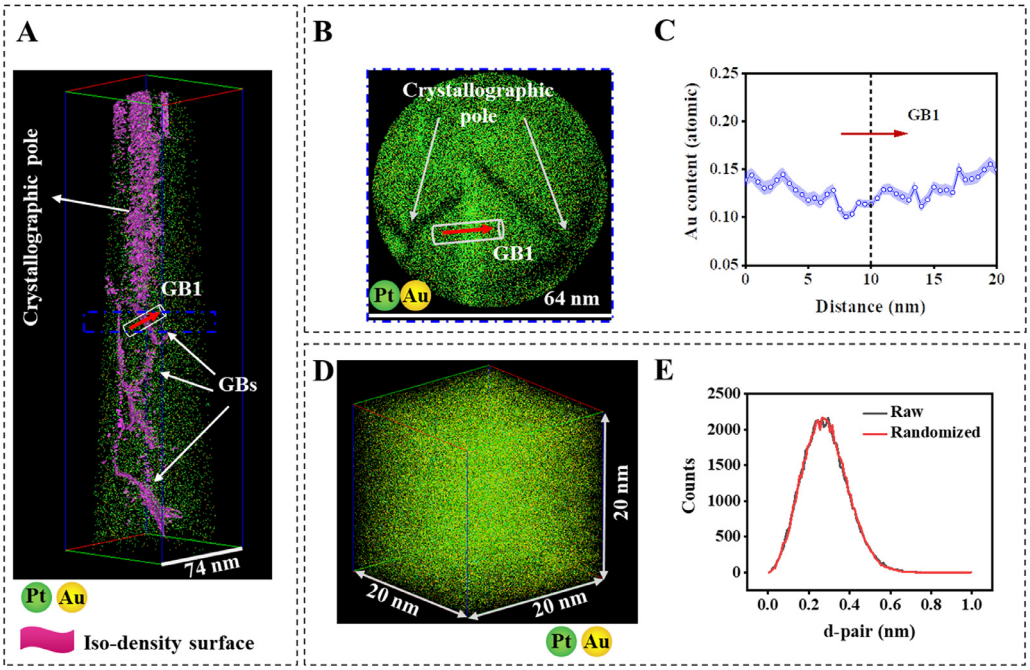

Fig. 3. **A** Atom map from APT of the Pt-11Au alloy with 120 /nm^3 iso-density surface embedded to highlight grain boundaries region. **B** atom map from a 5 nm thick cross-section to show one grain boundary **C** 1D concentration profile of the cylinder shown in A & B. The blue shading represents the statistical error associated with the calculation of the composition. **D** atom map cropped from the APT data of the as-deposited Pt-11Au sample. The size of the cropped cubic is 20 × 20 × 20 nm^3. **E** Au-Au nearest neighbor distributions. The randomized data is shown together with the raw data.

While APT is a destructive imaging technique where atoms are field evaporated and collected, by using different samples annealed at the same temperature but at different times, we are able to understand the general chemical partitioning evolution even though it is not the equivalent analyzed volume for all times at any particular temperature.

Within the 700 K/4 h sample, Fig. 4A, the onset of Au partitioning to the GBs is now apparent by the correlative comparison of Fig. 4Ai's PED map to Fig. 4Aii's atom map, where 0.15 atomic fraction Au isoconcentration surfaces delineate the GBs. The discontinuity of these iso-concentration surfaces in the GBs is a result of the inhomogeneity of the Au partitioning within the boundaries with this Au variation more apparent in the GB concentration map, Fig. 4Aiii. With an increase of GB misorientation, shown by the red arrow direction in Fig. 4Aiv, an increase of segregation can be noticed from the 2D GB composition map. While the grain size of this APT tip is visually larger than those seen in either the 24 and 720 h samples (Fig. 4B and C), this is consistent with the modest increase in the overall average grain size noted in the PED scans for this anneal, Fig. 2D, The modest increase in the average grain size is likely contributed to the grains coarsening before the solute is fully partitioned to the boundaries stunting the growth, which is consistent with prior reports for this alloy [40,48-50].Upon increasing the annealing time, the average grain size value does slightly refine and is likely a result of further solute partitioning to the GBs. Finally, we note that the concentration in the GBs at 4 h is relatively low, which would be expected to occur in the early stages of partitioning and/or decomposition where the concentration amplitudes have not increased.

Upon annealing for 24 h, the Au partitioning to the GBs becomes ever more apparent. The partitioning anisotropy noted between the different GB characters is revealed by the correlative comparison between the PED map, Fig. 4Bi, and the Au-enriched isoconcentration surfaces, Fig. 4Bii. While Au solute discontinuities exist within the GBs at 4 h, Fig. 4A, they are now much more pronounced resulting in clear, non-uniform segregation, Fig. 4Bii (with the arrow to guide the eye). Note that this particular atom map in Fig. 4Bii is based on a singular isoconcentration value, which can create continuous surfaces making some solute segregated regions appear unbroken.

Upon viewing the GB planes, the solute concentration discontinuities become even more apparent, Fig. 4Biii, with such types of discontinuities previously reported via electron microscopy [40,48]. But, beyond these prior works, which noted the anisotropic partitioning between the boundaries, we have expanded this information to directly link the segregation level to the GB character *and* its distribution on the GB-plane. From these results, it is clear that the onset of partitioning is spatially heterogeneous and Au does not uniformly decorate either the GBs or the individual boundary planes it resides on.

The alloy annealed to 720 h, with its cross-correlative comparison between the PED and APT datasets, is shown in Fig. 4C. This annealed sample retained the nanocrystalline grain structure with a {111} fiber texture, Fig. 4Ci. The EDXS map and the APT data, Fig. 4Cii-iii, reveal that Au-rich regions are located in HAGBs and/or at triple junctions. Comparing this to the prior 24 h anneal, Fig. 4B, the solute distribution has qualitatively become more heterogeneous. The APT results further expose that some clusters grew dominantly. In Fig. 4Ciii, a 5 nm diameter cylinder tube transverses a GB. The resulting one-dimensional (1D) concentration profile along the cylinder is plotted in Fig. 4Civ with this profile revealing a spatial variation in concentration, with the concentration being as high as 0.50 atomic fraction Au within the GB. The Au concentration within the interior of the grains is ~0.05 atomic fraction Au, indicating a segregation-induced solute depletion from the interior to the boundaries and no notable phase separation within the bulk interior.

While interfacial spinodal phase separation has been reported to be triggered in conjunction with segregation [27,28], with the above data suggesting an interfacial chemical decomposition in the GBs, direct evidence of confined GB spinodals are very difficult to experimentally realize. This is because of the need to identify the

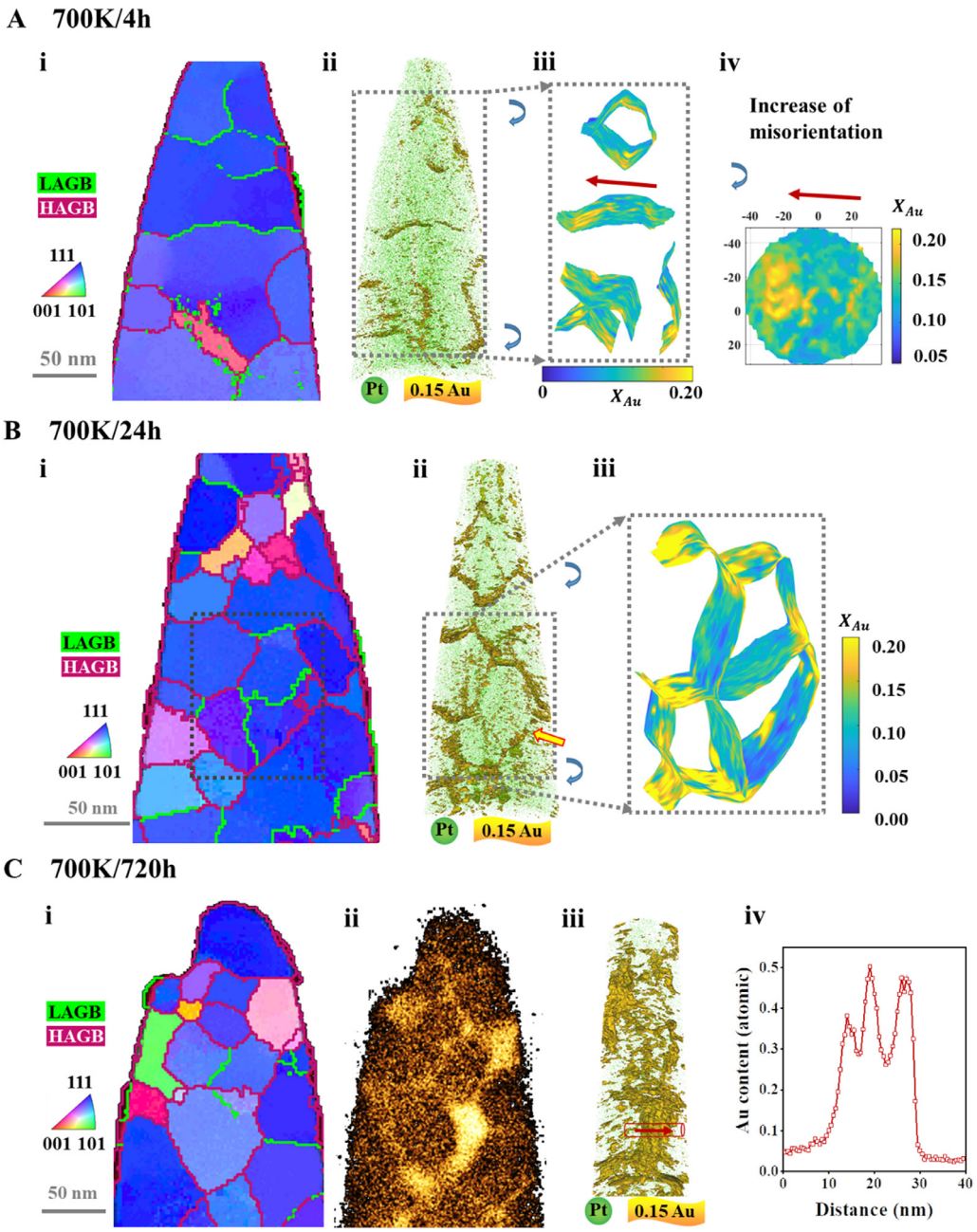

Fig. 4. **A** 700 K/4 h annealed Pt-11Au film – (i) PED orientation and grain boundary map (ii) Atom map reconstruction with 0.15 atomic fraction Au iso-concentration surface embedded (iii) Grain boundary concentration map that matches with a (iv) Selected LAGB for concentration mapping. **B** 700 K/24 h annealed Pt-11Au film – (i) PED orientation and GB map for the (ii) Atom map reconstruction with 0.15 atomic fraction Au iso-concentration surface embedded, the red-edge arrow indicating discontinuities within the GBs as a result of heterogeneous segregation (iii) GB Au concentration map that matches with (i) **C** 700 K/720 h annealed Pt-11Au film – (i) PED orientation and GB map (ii) EDXS map for the same tip (iii) Atom map reconstruction with 0.15 atomic fraction Au iso-concentration surface embedded (iv) Line profiles of the arrows shown in (iii).

decomposed low and high concentration areas throughout the entirety of the GB area. In particular, the low-dimensional GB spinodal fluctuations can interfere with the composition fluctuations because of its structural inhomogeneities [39]. To overcome this challenge for quantifying the interfacial phase separation behavior, we devised a reconstruction procedure, based on the concepts found in [51] to map the APT distribution of solute concentration within the GB-plane and is shown in Fig. 5A-C. These histograms have been generated from local compositions of many individual vertices within the GB-planes on the interface maps. For instance, Fig. 4Biii contains the local compositions of 4709 individual vertices on the GBs of which 1219 are for LAGBs and 3490 for HAGBs. Fig. 5B is its corresponding histogram for these GBs represented by the area fraction as a function of Au content. Similar distribution maps are extracted from the DPF simulations indicating low/high segregation level at the LAGBs/HAGBs, Fig. 5D-F respectively, and have been placed here for direct comparison to the experimental data with the details of the simulations discussed in the forthcoming Sec. 3.4.

For the experimental data, Fig. 5A and B are the histograms for 4 and 24 h annealing, respectively. We found that the LAGBs (green lines) appear to keep their narrower distribution near 0.11 atomic fraction, indicating less solute segregation while, during the same period, HAGBs (blue lines) reveal a broader distribution with

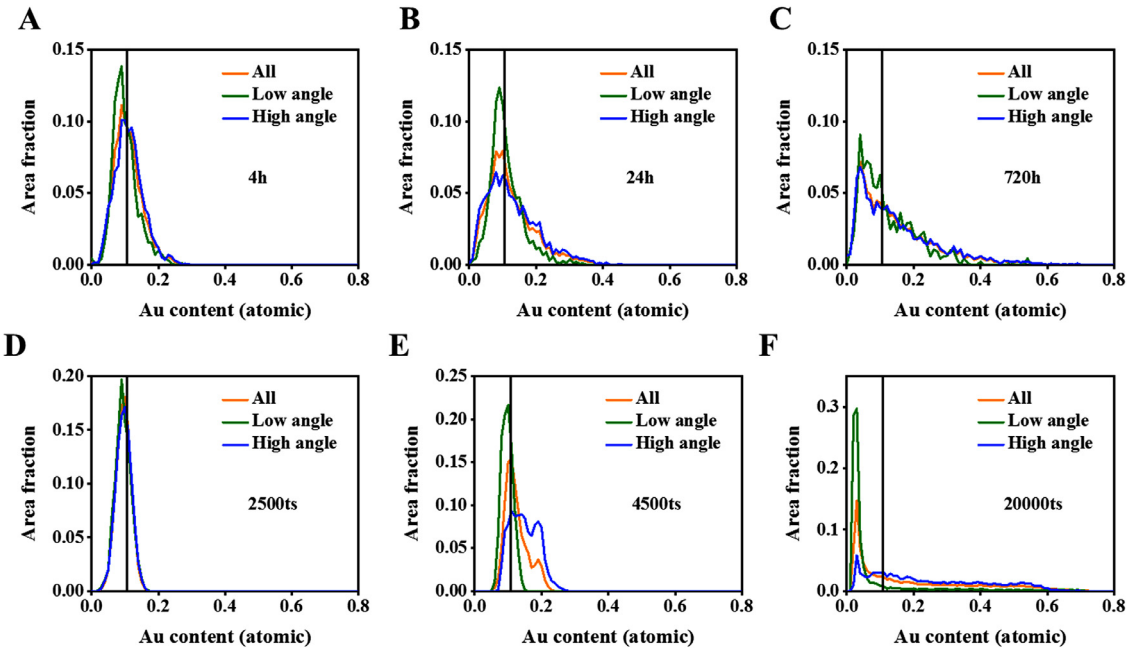

Fig. 5. The temporal evolution of solute Au atoms distributions *within* the GB for the Pt-11Au alloy annealed at 700 K, represented by area fraction as a function of Au content. **A – C** are for the APT measurement and **D – F** are 3D DPF simulation results at different time steps (ts).

a longer tail, expanded as high as 0.40 atomic fraction. These results suggest a larger driving force for segregation to the HAGBs. The simulation findings show a similar trend in Fig. 5D and E in which the uniform solute distribution grow wider with the HAGBs spreading larger than the LAGBs.

After the 720 h anneal, the tails in both the experimental and simulated histograms stretch to approximately 0.70 atomic fraction Au, Fig. 5C and F, with the peaks' maxima shifted to the left. Note that the vertical black line represents the nominal bulk composition, i.e., 0.11 atomic fraction Au. While the stretched tails signify the development of highly decorated GB areas with Au atoms, the peaks that shift to the left (i.e., lower Au content) reveal solute depletion in other GB areas. The broadened histograms over the concentration space also reflect the through-thickness concentration variations across the GBs' region, dictated by their intrinsic structural inhomogeneities, emphasizing the significance of gradient energy contributions that would be present in a spinodal decomposition reaction. With the ever rising compositional amplitude at the GBs (evident in the experimental data of Fig. 4), the changes in the histograms' peaks and tails in Fig. 5 mark an uphill diffusion from high-population, low-concentration to low-population, high-concentration areas within the GBs, which is characteristic of a spinodal separation. The combination of the APT results (Fig. 4) and in-plane GB composition analysis (Fig. 5) indicate the occurrence of the interfacial (GB) chemical decomposition in our nanocrystalline alloy with further phase-field simulation evidences for the GB spinodal behavior discussed in the following section.

3.4. Density-based Phase-Field Simulation of GB Segregation and Chemical Decomposition

Using the density-based free energy functional, Eq. 5, 3D simulations were devised to study the GB segregation and phase separation in the nanocrystalline Pt-11Au alloy. In order to have a close comparison with the experimental results, the experimentally measured PED orientation maps were imported as the initial grain structure to the DPF simulations. The experimental GB misorientations, denoted in Fig. 6A (taken from Fig. 4Bi), are mapped to the average GB densities ρ^{GB}'s in Fig. 6B, using a simple phenomenological relationship that assumes a monotonic reduction in the average GB density with misorientation angle increase (see Fig. 1). Despite its simplified nature, this treatment captures the general trend in GB density and energy as a function of misorientation angle sufficient for studying the relative GB segregation and interfacial phase separation behavior within our experimental nanocrystalline microstructure.

The temporal progression of the solute redistribution is shown by 12 snap-shots of the simulation, Fig. 6 Ci-Cxii, in a given cross-sectional view with a video available in the supplementary on-line information. The simulations reveal three stages of microstructure evolution: (1) solute redistribution, (2) interfacial chemical decomposition that reveals spinodal characteristics and (3) cluster ripening. We set up the initial simulation by evenly distributing the solute atoms in solution throughout the system to mimic the as-deposited Pt-11Au nanocrystalline alloy as shown in Fig. 3. The solute redistribution starts with a segregation among different GBs, with the HAGBs enriching at a faster rate than the other boundaries. This can be seen by comparing the boundary misorientation map (Fig. 6B) to the concentration maps (Fig. 6 Ci-Civ), where one can observe that the LAGBs enrich at a much lower rate and content. This was confirmed in the APT datasets as well, Fig. 4, where all HAGBs have a higher level of average solute segregation then the LAGBs.

With an increasing simulation time, the GBs exhibit characteristics of a spinodal decomposition event nominally seen in the bulk, *i.e.*, the composition fluctuation grows in amplitude with time. As reported in references [27,28], such spinodal events in defect structures have been previously noted in both grain boundaries and dislocations. In this nanocrystalline system, with its high population of GBs, there was ready access for the solute to first partition to these GBs where upon a chemical decomposition could then occur. If we look at the experimental sequence in Fig. 4 and the simulation snap-shots of Fig. 6 Ci-Cxii, we note an 'up-hill' diffusion of solute enrichment with a statistical distribution of concentration fluctuations (within the GBs) as a function of time, Fig. 5. This behavior mirrors a chemical evolution similar to spinodal decomposition. Note that in producing Fig. 5's histograms, the bulk informa-

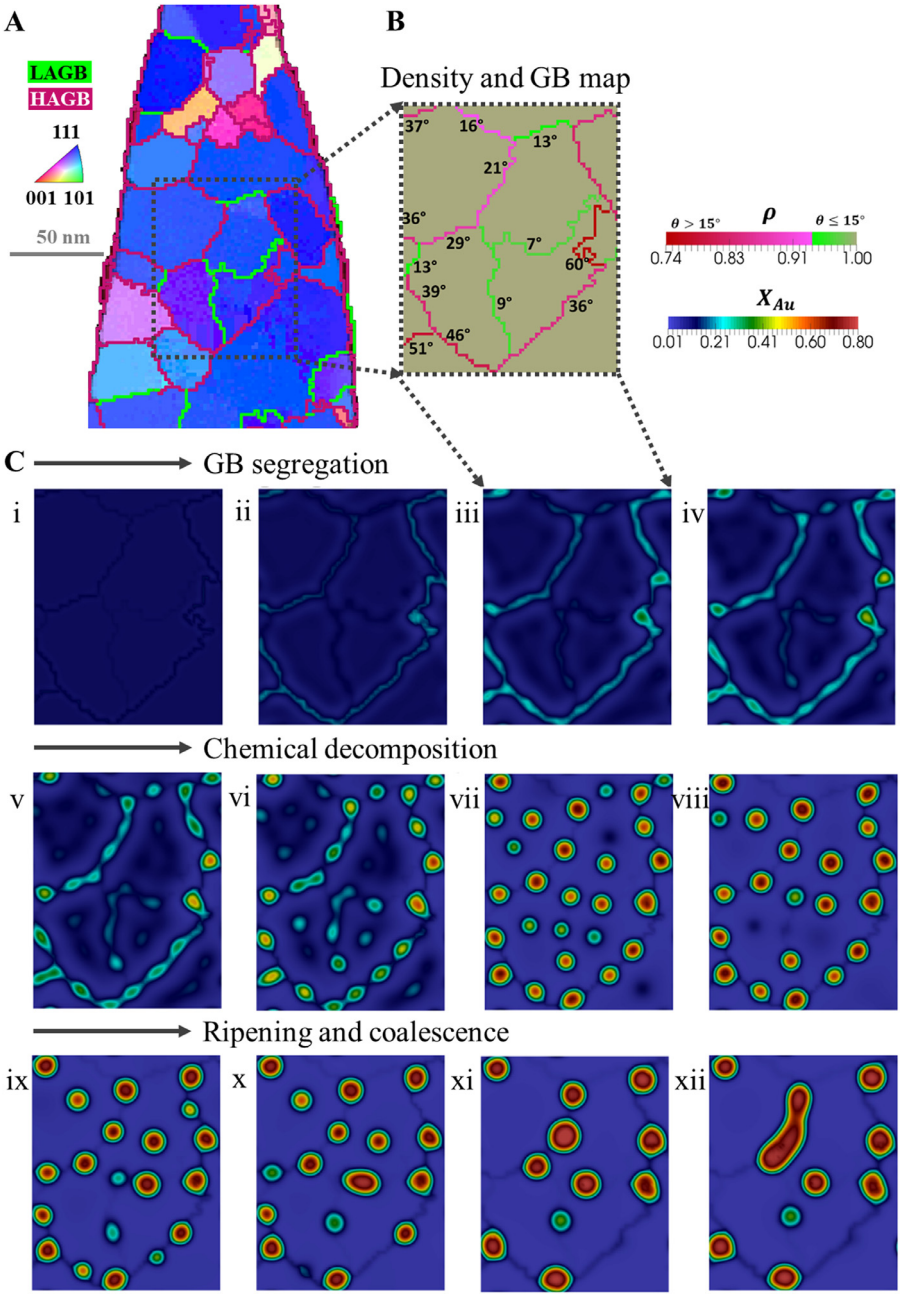

Fig. 6. **A** PED orientation and GB map for the 700 K/24 h annealed Pt-11Au film **B** The extracted GB map constructed to a density map that is then used to build the 3D simulation box and **C** 3D DPF simulation results of the temporal evolution of solute redistributions (12 sub-figures). A one-to-one comparison of the concentration (**C**) and density (**B**) fields reveal the density-dependent segregation and interfacial spinodal behavior.

tion is excluded. The widening of the histograms along the simulation time indicates that high-concentration sites start to form *within* the GBs while the population of the low-concentration sites grow larger (the peak in the histograms shift to the left).

Along with the competitive segregation and interfacial chemical decomposition, the Au solute content within the grain interior was continuously depleted. In the simulation, this depletion is evident by the change in the grain interiors' background color in Fig. 6 Ci-Cxii from dark-blue to light-blue as the solute segregates to the large population of GBs within the microstructure. With this depletion, the bulk composition for spinodal decomposition within the grain interiors now falls outside the miscibility region. The thermodynamic origins and consequences of these particular event is further discussed in the next section.

As the simulation continued, Fig. 6 Cix-Cxii, some of the phase-separated Au-enriched clusters coalesce together and grow by ripening. These coarsening clusters are often found at the triple junctions where the volume-averaged atomic density attains its minimum [1]. An implication of these Au-rich clusters is that they may act as a GB drag/pinning mechanism that additionally retards the grains from coarsening as noted in Fig. 2.

[1] If considering a coarse-grained unit volume across the system and averaging the density field, the lowest averaged densities will be realized around the triple junctions where several GBs of lower densities meet. This pattern is recognized by solute atoms due to the nonlocal solute-solute interactions (gradient energy terms) during the energy minimization, resulting in the localization of the solute clusters at the triple lines.

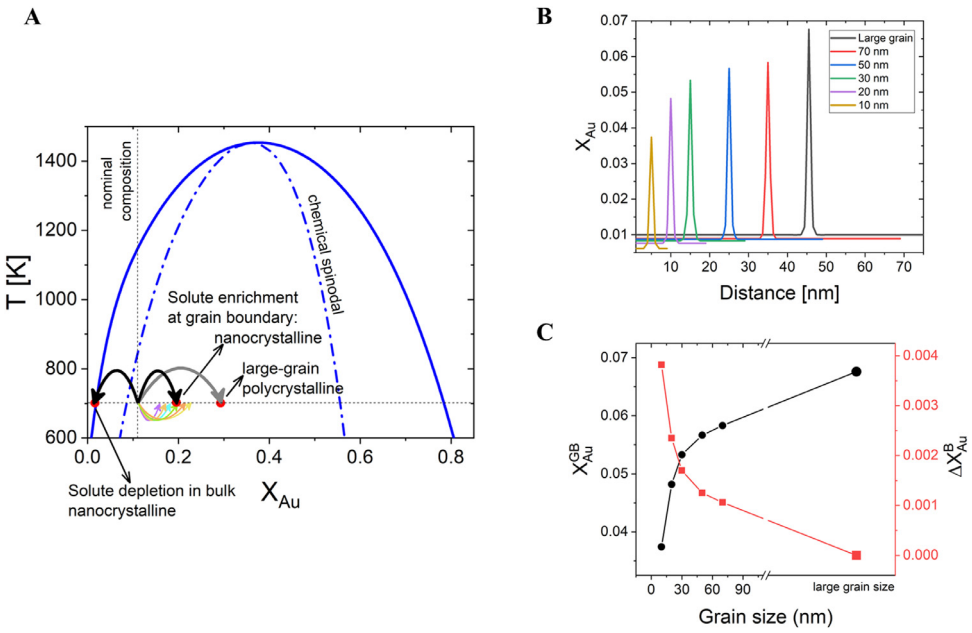

Fig. 7. **A** The phase diagram of Pt-Au system. Competitive segregation in nanocrystalline microstructure results in solute depletion in the interior grains and lower equilibrium segregation at GBs, compared to that in large-grain microstructures. The equilibrium GB segregation differs from GB to GB that is shown by colored curved arrows. We use the thermodynamic assessments from Grolier *et al.* [62] to obtain the phase diagram. Note that the colored arrows in A schematically indicate the spread in different grain boundaries' segregation behavior due to their diverse character. **B** Grain size-dependent equilibrium segregation profiles vs. the 'large-grain' case. **C** The maximum equilibrium GB concentration and the bulk solute depletion as a function of grain size for Pt-1Au at 700 K.

4. Discussion

Available thermodynamics data [62] confirms that the uniform solid solution Pt-11Au alloy (as-deposited condition) lies in the miscibility gap (spinodal region) of the bulk phase diagram, Fig. 7A. In our nanocrystalline microstructure, the bulk spinodal phase separation largely overlaps with the segregation processes among the nanometer distanced GBs which redefines the concentration landscape. From the experimental and simulation results, we have determined that the Au partitions to these GBs. This partitioning occurs in a heterogeneous manner in terms of both concentration level and solute distribution within the GBs. These are evidenced in Figs. 4 and 6. Furthermore, along with an ever-increasing composition of the GBs, we note an uphill diffusion of Au atoms *within* the GBs, as analyzed in Fig. 5, that all together confirm the GB chemical decomposition in our nanocrystalline alloy.

This type of GB spinodal behavior has been evidenced in other materials using different experimental methods [27,69,70]. In contrast to these previous reports, which focus on the GB spinodal behavior in large-grain size microstructures, we have addressed it in a nanocrystalline microstructure where several critical differences can now be noted. The large population of GBs (related to the grain size in the system) results in a solute depletion within the bulk grain interior that couples to the solute segregation to the GBs and the subsequent chemical separation phenomena within the GBs. To single-out this grain size effect, solute partitioning was studied using the DPF model for a Pt-1Au (0.01 atomic fraction Au) alloy. Fig. 7B shows the equilibrium segregation profiles. We chose Pt-1Au at 700 K (in the single phase region of the phase diagram) so that the grain size effect can be demonstrated without interference with the spinodal decomposition. For a single flat GB, with a periodic boundary condition, the simulation box size represents the spacing between the GBs, *i.e.*, the grain size. A large grain scenario is then emulated by applying a fixed concentration boundary condition parallel to the GB-plane. Here the 'large-grain' refers to a grain size such that the grain interior's bulk composition is not influenced by the segregation, *i.e.*, the number of segregated solutes is negligible compared to the total solutes in the entire system. We found that the equilibrium bulk and GB compositions shift as a result of grain size such that for smaller grain sizes (larger GB populations), the equilibrium GB segregation is suppressed and the abutting bulk phase is solute depleted. Fig. 7C reveals this corresponding GB/bulk composition/depletion as a function of grain size. This grain size effect has a decisive impact on the solute redistribution within the nanometer-sized grain structures. Upon segregation, the interior bulk portions of the grains become solute depleted as clearly shown from Fig. 4Civ (experiment) and Fig. 6Cix-xii (simulation). This depletion shifts the concentration within the grain interior outside the miscibility gap making the interior composition no longer thermodynamically driven to spinodally decompose. In contrast, a coarse grain structure can still retain sufficient solute within its bulk interior, even as some solute partitions to its GBs, enabling its interior composition to still be placed in a thermodynamic condition for spinodal decomposition. As these solutes enrich the GBs through segregation, the GBs become compositionally shifted towards a thermodynamic regime that places it in a condition to undergo spinodal decomposition. The vast diversity of the GB characters within a nanocrystalline microstructure can now impact this segregation and GB chemical decomposition behavior, especially recognizing that the GBs are just nanometer distances apart. These consequences are better understood based on a comparison between the bulk and GB chemical potentials.

The chemical potential of a GB includes nonlocal gradient energy contributions stemming from the free energy functional shown in Eq. (5). Neglecting these gradient terms and focusing on the local energy contributions, Fig. 8 compares the chemical potentials of Au in the Pt-Au system for the bulk and three different GBs at 700 K, with each of these boundaries represented by a different density. For any given alloy composition on the bulk curve, the difference in the GB and bulk chemical potentials represents the driving forces for solute segregation to that GB. From Fig. 8, it is clear that the driving force for segregation is higher for HAGBs (lower GB densities). This explains the larger segrega-

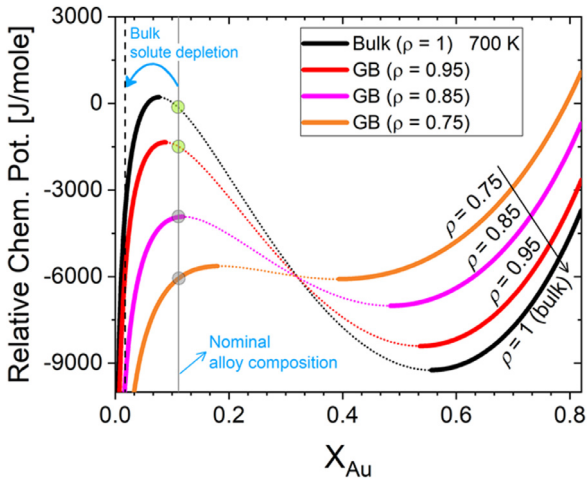

Fig. 8. Chemical potentials of Au in the Pt-Au system for bulk ($\rho = 1$) and different GBs ($\rho < 1$) based on the density-based free energy description. We use the thermodynamic assessments from Grolier *et al.* [62]. The unstable (spinodal) ranges are shown as doted-lines. For lower GB densities (here $\rho^{GB} = 0.85$ or 0.75), the Pt-11Au alloy appears outside the spinodal region.

tions to the HAGBs compared to the LAGBs observed in both experiments (Fig. 4) and simulations (Fig. 6) particularly present in the early time sequences.

Fig. 8 also reveals that for GBs, the unstable low-dimensional, chemical decomposition regions (the dotted parts on the chemical potential curves) becomes smaller. This means that the barrier-free chemical decomposition has its own characteristics for the GBs, which are different from that of the bulk. Additionally, the chemical potential curves show that the smaller the GB density, the narrower the miscibility gaps for the GB; therefore, a greater concentration of the solute is required to activate the interfacial chemical decomposition within that boundary. For instance, a HAGB with the lowest density in Fig. 8 requires up to 0.18 atomic fraction Au in order to begin the GB chemical decomposition, whilea LAGB with higher densities (closer to 1), the initial alloy with 0.11 atomic fraction Au is already well within the miscibility gap.

Expectedly, when two or more GBs with various GB densities are present, a competitive partitioning and interfacial chemical decomposition can take place. The size effects discussed in Fig. 7A-C results in a solute depletion and lesser chance for spinodal decomposition in the bulk. Conversely, since the concentration fluctuations grow larger upon segregation at the GBs, the Au-enriched GBs become far more amenable to initiate chemical decomposition (see Figs. 4 and 6). Interestingly, our simulations in Fig. 6 reveal that both HAGBs and LAGBs undergo the chemical decomposition around the same time. This can be explained now by the two concurrent effects, *i.e.*, the high driving forces for solute segregation to the HAGBs enriching themselves rapidly up into the edge of their chemical decomposition region, while, for the LAGBs, their chemical decomposition regions are larger and allow for an interfacial composition separation with no or little prior segregation (Fig. 8).

From our experimental and modeling results, it becomes clear that both segregation and low-dimensional GB chemical decomposition phenomena will depend upon the GB population and character. These outcomes are particularly relevant in that spinodal decomposition is a barrier-free phase transition where defects, like GBs, are usually ignored – in contrast to the classical nucleation scenario where such defects are considered for explaining where and how nucleation reactions occur, *e.g.,* in the various heterogeneous nucleation models. Our results show that GBs can indeed influence the chemical decomposition process by having their own planar characteristics that, in the Pt-Au case, require a higher solute concentration to enter the GB-specific low-dimensional chemical decomposition regimes (Fig. 8). In this sense, GBs tend to delay the barrier-free spinodal phase separation until they reach their appropriate segregation level. As a result, the accommodation of solute atoms by certain GB types can be thought as a potential tunable variable for phase separation in nanocrystalline alloys where a miscibility gap exists.

5. Conclusions

In summary, by combining near-atomic tomographic and microscopy studies with a density-based thermodynamic model and phase-field simulation, the grain size-dependent, competitive GB segregation and phase separation behavior in nanocrystalline Pt-11Au was elucidated. We found that microstructural defects (*i.e.*, different types of GBs) can have their own critical concentrations to initiate chemical decomposition which then alters the spinodal decomposition pathway in nanocrystalline alloys. For nanocrystalline materials with a miscibility gap, two effects where noted. First, GBs take solutes from the bulk, driving the bulk interior of the grains towards a single-phase region where spinodal decomposition, within the bulk interior, does not occur. And second, GBs (especially HAGBs) accommodate more solute and show less tendency for chemical decomposition themselves until a higher solute content is reached (Fig. 8). The temporal evolution of the solute distribution revealed by cross-correlative APT and PED confirms these model predictions, while the model provided the ability to reveal the formation mechanisms of the discontinuities seen to occur in the experimentally characterized GBs.

Understanding the solute redistribution and the kinetic pathways where solute enrichment within GBs occurs provides outlooks on nanocrystalline stability considerations. Specifically, we found that HAGBs have a higher driving force for solutes to segregate to, but require a higher amount of solutes for triggering a chemical decomposition. Their transient evolution drives towards a discontinuity of solute clusters that would promote a kinetic pinning effect for nanocrystalline stabilization, as the grain size did not coarsen within the annealing time of our study as well as others [48]. These findings suggest that engineering a high fraction of general HAGBs would assist in producing a more homogeneous segregation network for the stabilization of nanocrystalline alloys whose elements are immiscible and exhibit a miscibility gap.

Contribution statements

X.Z., R.D.K., D.R. and G.B.T. conceived of the presented ideas. B.L.B. and B.G.C. provided the as-deposited Pt-Au sample. X.Z. conducted the annealing experiments and analytical characterization. R.D.K. developed the density-based phase-field theory and performed the simulations. All authors provided critical feedback and helped shape the research, analysis and discussion.

Data and materials availability

All data is available in the manuscript.

Declaration of Competing Interest

Authors declare no competing interests.

Acknowledgments

X.Z. and G.B.T. gratefully recognize the National Science Foundation-DMR-1709803 for support of this research. X.Z. also

recognizes support by Alexander von Humboldt-Stiftung. R.D.K. acknowledges the financial support from German Research Foundation (DFG) within the Heisenberg programme, project DA 1655/2-1. B.L.B. and B.G.C. acknowledge US Department of Energy, Office of Science, Materials Sciences and Engineering Division. We \thank Dr. Alisson Kwiatkowski da Silva for technical guidance in the APT analysis.

Supplementary materials

Supplementary material associated with this article can be found, in the online version, at doi:10.1016/j.actamat.2021.117054.

References

[1] W. Sun, Y. Zhu, R. Marceau, L. Wang, Q. Zhang, X. Gao, C. Hutchinson, Precipitation strengthening of aluminum alloys by room-temperature cyclic plasticity, Science 363 (6430) (2019) 972–975.
[2] B. He, B. Hu, H. Yen, G. Cheng, Z. Wang, H. Luo, M. Huang, High dislocation density–induced large ductility in deformed and partitioned steels, Science 357 (6355) (2017) 1029–1032.
[3] K. Darling, M. Rajagopalan, M. Komarasamy, M. Bhatia, B. Hornbuckle, R. Mishra, K. Solanki, Extreme creep resistance in a microstructurally stable nanocrystalline alloy, Nature 537 (7620) (2016) 378–381.
[4] S.H. Jiang, H. Wang, Y. Wu, X.J. Liu, H.H. Chen, M.J. Yao, B. Gault, D. Ponge, D. Raabe, A. Hirata, M.W. Chen, Y.D. Wang, Z.P. Lu, Ultrastrong steel via minimal lattice misfit and high-density nanoprecipitation, Nature 544 (7651) (2017) 460–464.
[5] M.A. Gibson, C.A. Schuh, Segregation-induced changes in grain boundary cohesion and embrittlement in binary alloys, Acta Mater 95 (2015) 145–155.
[6] Z. Lei, X. Liu, Y. Wu, H. Wang, S. Jiang, S. Wang, X. Hui, Y. Wu, B. Gault, P. Kontis, D. Raabe, L. Gu, Q. Zhang, H. Chen, H. Wang, J. Liu, K. An, Q. Zeng, T.-G. Nieh, Z. Lu, Enhanced strength and ductility in a high-entropy alloy via ordered oxygen complexes, Nature 563 (7732) (2018) 546–550.
[7] J.P. Buban, K. Matsunaga, J. Chen, N. Shibata, W.Y. Ching, T. Yamamoto, Y. Ikuhara, Grain Boundary Strengthening in Alumina by Rare Earth Impurities, Science 311 (2006) 212–215.
[8] N.J. Petch, The Cleavage Strength of Polycrystals, J. Iron Steel Inst., London 174 (1953) 25–28.
[9] E.O. Hall, The Deformation and Ageing of Mild Steel: III Discussion of Results, Proc. Phys. Soc., London, Sect. B 64 (9) (1951) 747–753.
[10] H. Gleiter, Nanocrystalline materials, Prog. Mater. Sci. 33 (4) (1989) 223–315.
[11] J. Weissmüller, Alloy effects in nanostructures, Nanostruct. Mater. 3 (1993) 261–272.
[12] T. Chookajorn, H.A. Murdoch, C.A. Schuh, Design of Stable Nanocrystalline Alloys, Science 337 (6097) (2012) 951–954.
[13] P.-G. De Gennes, F. Brochard-Wyart, D. Quéré, Capillarity and wetting phenomena: drops, bubbles, pearls, waves, Springer Science & Business Media, 2013.
[14] R. Kirchheim, Grain coarsening inhibited by solute segregation, Acta Mater 50 (2) (2002) 413–419.
[15] P. Lejcek, Grain Boundary Segregation in Metals, 2010.
[16] H.A. Murdoch, C.A. Schuh, Estimation of grain boundary segregation enthalpy and its role in stable nanocrystalline alloy design, J. Mater. Res. 28 (16) (2013) 2154–2163.
[17] H.A. Murdoch, C.A. Schuh, Stability of binary nanocrystalline alloys against grain growth and phase separation, Acta Mater 61 (6) (2013) 2121–2132.
[18] R.A. Andrievski, Review of thermal stability of nanomaterials, J. Mater. Sci. 49 (4) (2014) 1449–1460.
[19] K.A. Darling, M.A. Tschopp, B.K. VanLeeuwen, M.A. Atwater, Z.K. Liu, Mitigating grain growth in binary nanocrystalline alloys through solute selection based on thermodynamic stability maps, Comput. Mater. Sci. 84 (2014) 255–266.
[20] W.T. Xing, A.R. Kalidindi, C.A. Schuh, Preferred nanocrystalline configurations in ternary and multicomponent alloys, Scr. Mater. 127 (2017) 136–140.
[21] C.S. Smith, Introduction to Grains, Phases, and Interfaces-an Interpretation of Microstructure, Trans. Metall. Soc. AIME 175 (1948) 15–51.
[22] E. Nes, N. Ryum, O. Hunderi, On The Zener Drag, Acta Metall 33 (1) (1985) 11–22.
[23] J.W. Cahn, On Spinodal Decomposition, Acta Metall 9 (9) (1961) 795–801.
[24] D.A. Porter, K.E. Easterling, M. Sherif, Phase Transformations in Metals and Alloys, CRC Press, New York, 2009 Third Edition (Revised Reprint.
[25] W.K. Choo, J. Kim, J. Yoon, Microstructural change in austenitic Fe-30.0 wt% Mn-7.8 wt% Al-1.3 wt% C initiated by spinodal decomposition and its influence on mechanical properties, Acta Mater 45 (12) (1997) 4877–4885.
[26] J.J. Reinosa, F. Rubio-Marcos, E. Solera, M.A. Bengochea, J.F. Fernández, Sintering behaviour of nanostructured glass-ceramic glazes, Ceramics International 36 (6) (2010) 1845–1850.
[27] A.K. da Silva, D. Ponge, Z. Peng, G. Inden, Y. Lu, A. Breen, B. Gault, D. Raabe, Phase nucleation through confined spinodal fluctuations at crystal defects evidenced in Fe-Mn alloys, Nat. Commun. 9 (2018) 1137.
[28] R. Darvishi Kamachali, A. Kwiatkowski da Silva, E. McEniry, D. Ponge, B. Gault, J. Neugebauer, D. Raabe, Segregation-assisted spinodal and transient spinodal phase separation at grain boundaries, npj Computational Materials 6 (1) (2020) 191.
[29] M. Herbig, D. Raabe, Y.J. Li, P. Choi, S. Zaefferer, S. Goto, Atomic-Scale Quantification of Grain Boundary Segregation in Nanocrystalline Material, Phys. Rev. Lett. 112 (12) (2014) 126103.
[30] X. Zhou, X.-x. Yu, T. Kaub, R.L. Martens, G.B. Thompson, Grain Boundary Specific Segregation in Nanocrystalline Fe(Cr), Sci. Rep. 6 (2016) 34642.
[31] V.J. Araullo-Peters, B. Gault, S.L. Shrestha, L. Yao, M.P. Moody, S.P. Ringer, J.M. Cairney, Atom probe crystallography: Atomic-scale 3-D orientation mapping, Scr. Mater. 66 (11) (2012) 907–910.
[32] B.M. Jenkins, J.O. Douglas, H.M. Gardner, D. Tweddle, A. Kareer, P.S. Karamched, N. Riddle, J.M. Hyde, P.A.J. Bagot, G.R. Odette, M.P. Moody, A more holistic characterisation of internal interfaces in a variety of materials via complementary use of transmission Kikuchi diffraction and Atom probe tomography, Appl. Surf. Sci. 528 (2020) 147011.
[33] R.Darvishi Kamachali, A model for grain boundary thermodynamics, RSC Advances 10 (2020) 26728–26741.
[34] R.Q. Wu, A.J. Freeman, G.B. Olson, First Principles Determination of the Effects of Phosphorus and Boron on Iron Grain-Boundary Cohesion, Science 265 (5170) (1994) 376–380.
[35] S. Yang, N. Zhou, H. Zheng, S.P. Ong, J. Luo, First-Order Interfacial Transformations with a Critical Point: Breaking the Symmetry at a Symmetric Tilt Grain Boundary, Phys. Rev. Lett. 120 (8) (2018) 085702.
[36] L. Feng, Y. Rao, M. Ghazisaeidi, M.J. Mills, Y. Wang, Quantitative prediction of Suzuki segregation at stacking faults of the γ' phase in Ni-base superalloys, Acta Mater 200 (2020) 223–235.
[37] B. Sadigh, P. Erhart, A. Stukowski, A. Caro, E. Martinez, L. Zepeda-Ruiz, Scalable parallel Monte Carlo algorithm for atomistic simulations of precipitation in alloys, Phys. Rev. B 85 (18) (2012) 184203.
[38] M. Wagih, C.A. Schuh, Spectrum of grain boundary segregation energies in a polycrystal, Acta Mater 181 (2019) 228–237.
[39] A. Gupta, X.Y. Zhou, G.B. Thompson, G.J. Tucker, Role of grain boundary character and its evolution on interfacial solute segregation behavior in nanocrystalline Ni-P, Acta Mater 190 (2020) 113–123.
[40] C. O'Brien, C. Barr, P. Price, K. Hattar, S. Foiles, Grain boundary phase transformations in PtAu and relevance to thermal stabilization of bulk nanocrystalline metals, J. Mater. Sci. 53 (4) (2018) 2911–2927.
[41] N. Ma, S.A. Dregia, Y. Wang, Solute segregation transition and drag force on grain boundaries, Acta Mater 51 (13) (2003) 3687–3700.
[42] M. Tang, W.C. Carter, R.M. Cannon, Grain Boundary Transitions in Binary Alloys, Phys. Rev. Lett. 97 (7) (2006) 075502.
[43] K. Grönhagen, J. Ågren, Grain-boundary segregation and dynamic solute drag theory—A phase-field approach, Acta Mater 55 (3) (2007) 955–960.
[44] F. Abdeljawad, S.M. Foiles, Stabilization of nanocrystalline alloys via grain boundary segregation: A diffuse interface model, Acta Mater 101 (2015) 159–171.
[45] Y. Mishin, Solute drag and dynamic phase transformations in moving grain boundaries, Acta Mater 179 (2019) 383–395.
[46] R. Shi, T.W. Heo, B.C. Wood, Y. Wang, Critical nuclei at hetero-phase interfaces, Acta Mater 200 (2020) 510–525.
[47] X. Zhou, J.D. Schuler, C.M. Grigorian, D. Tweddle, T.J. Rupert, L. Li, G.B. Thompson, Influence and comparison of contaminate partitioning on nanocrystalline stability in sputter-deposited and ball-milled Cu–Zr alloys, J. Mater. Sci. 55 (2020) 16758–16779.
[48] P. Lu, F. Abdeljawad, M. Rodriguez, M. Chandross, D.P. Adams, B.L. Boyce, B.G. Clark, N. Argibay, On the thermal stability and grain boundary segregation in nanocrystalline PtAu alloys, Materialia 6 (2019) 100298.
[49] N.M. Heckman, S.M. Foiles, C.J. O'Brien, M. Chandross, C.M. Barr, N. Argibay, K. Hattar, P. Lu, D.P. Adams, B.L. Boyce, New nanoscale toughening mechanisms mitigate embrittlement in binary nanocrystalline alloys, Nanoscale 10 (45) (2018) 21231–21243.
[50] C.M. Barr, S.M. Foiles, M. Alkayyali, Y. Mahmood, P.M. Price, D.P. Adams, B.L. Boyce, F. Abdeljawad, K. Hattar, The role of grain boundary character in solute segregation and thermal stability of nanocrystalline Pt–Au, Nanoscale 13 (6) (2021) 3552–3563.
[51] P. Felfer, B. Scherrer, J. Demeulemeester, W. Vandervorst, J.M. Cairney, Mapping interfacial excess in atom probe data, Ultramicroscopy 159 (2015) 438–444.
[52] L. Yao, S.P. Ringer, J.M. Cairney, M.K. Miller, The anatomy of grain boundaries: Their structure and atomic-level solute distribution, Scr. Mater. 69 (8) (2013) 622–625.
[53] F. Abdeljawad, P. Lu, N. Argibay, B.G. Clark, B.L. Boyce, S.M. Foiles, Grain boundary segregation in immiscible nanocrystalline alloys, Acta Mater 126 (2017) 528–539.
[54] L. Li, R. Darvishi Kamachali, Z. Li, Z. Zhang, Grain boundary energy effect on grain boundary segregation in an equiatomic high-entropy alloy, Phys. Rev. Mater. 4 (5) (2020) 053603.
[55] L. Wang, R.Darvishi Kamachali, Density-based grain boundary phase diagrams: Application to Fe-Mn-Cr, Fe-Mn-Ni, Fe-Mn-Co, Fe-Cr-Ni and Fe-Cr-Co alloy systems, Acta Mater 207 (2021) 116668.
[56] G. Gottstein, L.S. Shvindlerman, Grain Boundary Migration in Metals: Thermodynamics, Kinetics, Applications, Taylor & Francis, New York, 1999.
[57] H.B. Aaron, G.F. Bolling, Free volume as a criterion for grain boundary models, Surf. Sci. 31 (1972) 27–49.
[58] H.B. Aaron, G.F. Bolling, Free volume as a guide to grain boundary phenomena, Scr. Metall. 6 (7) (1972) 553–562.
[59] The NIST repository for interatomic potentials. URL https://www.ctcms.nist.gov/potentials.).

[60] V.V. Bulatov, B.W. Reed, M. Kumar, Grain boundary energy function for fcc metals, Acta Mater 65 (2014) 161–175.
[61] J.W. Cahn, J.E. Hilliard, Free Energy of a Nonuniform System. I. Interfacial Free Energy, J. Chem. Phys. 28 (2) (1958) 258–267.
[62] V. Grolier, R. Schmid-Fetzer, Experimental study of Au-Pt-Sn phase equilibria and thermodynamic assessment of the Au-Pt and Au-Pt-Sn systems, J. Electron. Mater. 37 (3) (2008) 264–278.
[63] Y. Liu, J. Wang, Y. Du, G. Sheng, Z. Long, L. Zhang, Phase boundary migration, Kirkendall marker shift and atomic mobilities in fcc Au–Pt alloys, Calphad 36 (2012) 94–99.
[64] L.T. Stephenson, M.P. Moody, P.V. Liddicoat, S.P. Ringer, New techniques for the analysis of fine-scaled clustering phenomena within atom probe tomography (APT) data, Microsc. Microanal. 13 (6) (2007) 448–463.
[65] E. Marquis, J. Hyde, Applications of atom-probe tomography to the characterisation of solute behaviours, Mater. Sci. Eng., R 69 (4-5) (2010) 37–62.
[66] A.J.W. Moore, The structure of atomically smooth spherical surfaces, J. Phys. Chem. Solids 23 (7) (1962) 907–912.
[67] M. Miller, K., The effects on local magnification and trajectory aberrations on atom probe analysis, J. Phys. Colloques 48 (C6) (1987) C6-565-570.
[68] F. Vurpillot, A. Bostel, D. Blavette, Trajectory overlaps and local magnification in three-dimensional atom probe, Appl. Phys. Lett. 76 (21) (2000) 3127–3129.
[69] L.L. Li, Z.M. Li, A.K. da Silva, Z.R. Peng, H. Zhao, B. Gault, D. Raabe, Segregation-driven grain boundary spinodal decomposition as a pathway for phase nucleation in a high-entropy alloy, Acta Mater 178 (2019) 1–9.
[70] S. Rajeshwari K, S. Sankaran, K.C. Hari Kumar, H. Rösner, M. Peterlechner, V.A. Esin, S. Divinski, G. Wilde, Grain boundary diffusion and grain boundary structures of a Ni-Cr-Fe- alloy: Evidences for grain boundary phase transitions, Acta Mater 195 (2020) 501–518.